

## A GLOBAL VIEW OF GRAVITY WAVES IN THE MARTIAN ATMOSPHERE INFERRED FROM A HIGH-RESOLUTION GENERAL CIRCULATION MODEL

TAKESHI KURODA<sup>1,2</sup>, ALEXANDER S. MEDVEDEV<sup>2,3</sup>, ERDAL YİĞİT<sup>4,2</sup>, AND PAUL HARTOGH<sup>2</sup>

ACCEPTED FOR PUBLICATION IN GEOPHYSICAL RESEARCH LETTERS: October 24, 2015

## ABSTRACT

Global characteristics of the small-scale gravity wave (GW) field in the Martian atmosphere obtained from a high-resolution general circulation model (GCM) are presented for the first time. The simulated GW-induced temperature variances are in a good agreement with available radio occultation data in the lower atmosphere between 10 and 30 km. The model reveals a latitudinal asymmetry with stronger wave generation in the winter hemisphere, and two distinctive sources of GWs: mountainous regions and the meandering winter polar jet. Orographic GWs are filtered while propagating upward, and the mesosphere is primarily dominated by harmonics with faster horizontal phase velocities. Wave fluxes are directed mainly against the local wind. GW dissipation in the upper mesosphere generates body forces of tens of  $\text{m s}^{-1} \text{ sol}^{-1}$ , which tend to close the simulated jets. The results represent a realistic surrogate for missing observations, which can be used for constraining GW parameterizations and validating GCM simulations.

*Subject headings:* Mars atmosphere, Gravity waves, General Circulation Model, High-resolution modeling

## 1. INTRODUCTION

The dynamical importance of small-scale gravity waves (GWs) has been well recognized in the terrestrial middle atmosphere (see the extensive review paper of [Fritts and Alexander 2003](#)) and upper atmosphere (e.g., see the recent review of [Yiğit and Medvedev 2015](#)). On Mars, GWs are generated by flow over much rougher than on Earth topography, by strong convection, and volatile instabilities of weather systems. Amplitudes of Martian GWs are, generally, larger than those in the lower atmosphere of Earth (e.g., [Creasey et al. 2006a](#); [Wright 2012](#)) and in the thermosphere ([Creasey et al. 2006b](#); [Fritts et al. 2006](#)). Upward propagating and ultimately dissipating GWs deposit a substantial amount of momentum and produce heating and cooling in the Martian middle atmosphere (50–100 km) and thermosphere (above 100 km) ([Medvedev and Yiğit 2012](#)). Using the Mars Global Surveyor (MGS) radio occultation data, [Ando et al. \(2012\)](#) have demonstrated that spectral amplitudes of small-scale GWs below  $\sim 40$  km drop off with respect to their vertical wavenumbers according to the theoretical saturation and power law dependence of  $-3$  slope, which implies a transfer of wave energy and momentum to the mean flow. Based on the MGS accelerometer data, [Fritts et al. \(2006\)](#) have found significant body forcing by GWs in the lower thermosphere.

The Martian atmosphere is approximately 100 times less dense than the terrestrial one. Accordingly, molecular viscosity is to the same degree larger on Mars, and damping by molecular diffusion and thermal conduction must be taken into account when GW propagation is

considered, as in Earth’s thermosphere. GWs of interest have horizontal wavelengths usually smaller than the conventional resolution of general circulation models (GCMs), and, thus, their effects have to be parameterized. [Medvedev et al. \(2011a\)](#) applied the nonlinear spectral parameterization of small-scale GWs of [Yiğit et al. \(2008\)](#) to the output of the Mars Climate Database ([González-Galindo et al. 2009](#)) and demonstrated that dynamical effects of these waves in the Martian lower thermosphere are very large and, therefore, cannot be ignored. This parameterization was specifically developed for “whole atmosphere” GCMs, and was extensively utilized in numerous GW studies in the context of Earth’s middle atmosphere and thermosphere ([Yiğit et al. 2009, 2012, 2014](#); [Yiğit and Medvedev 2009, 2012](#)). With the parameterization interactively implemented into the Max Planck Institute Martian GCM (MGC) ([Hartogh et al. 2005](#); [Hartogh et al. 2007](#); [Medvedev and Hartogh 2007](#)), [Medvedev et al. \(2011b\)](#) have shown that GWs play a very important role in the dynamics of the middle and upper atmosphere of Mars. They close, and even reverse, the zonal jets, enhance the meridional circulation and middle atmosphere polar warmings, facilitate a formation of CO<sub>2</sub> ice clouds ([Yiğit et al. 2015](#)), and modulate the upper atmospheric response to dust storms ([Medvedev et al. 2013](#)). GW-induced cooling is as strong in the mesosphere and thermosphere as the major radiative cooling mechanism – the radiative transfer in the IR bands of CO<sub>2</sub> molecules ([Medvedev et al. 2015](#)), – and can explain the observed temperatures in the lower thermosphere ([Medvedev and Yiğit 2012](#)).

GW parameterizations assume a spectrum of wave harmonics at a certain source level in the lower atmosphere in order to represent GW generation and activity. Accurate estimates of GW momentum fluxes have, therefore, been recognized as an essential task in the Earth climate studies. However, with the concerted efforts and numerous observational campaigns ([Alexander et al. 2010](#)), the

<sup>1</sup> Department of Geophysics, Tohoku University, Sendai, Japan.

<sup>2</sup> Max Planck Institute for Solar System Research, Göttingen, Germany.

<sup>3</sup> Institute of Astrophysics, Georg-August University, Göttingen, Germany.

<sup>4</sup> Department of Physics and Astronomy, George Mason University, Fairfax, Virginia, USA.

global picture of GWs is still beyond our reach even on Earth. On Mars, this goal is even farther away. The progress with numerical modeling has allowed to circumvent this problem to a certain degree by utilizing high-resolution (GW-resolving) GCMs. They are now being increasingly used in Earth studies for the interpretation and validation of observations and constraining parameterizations (e.g., [Watanabe et al. 2008](#); [Sato et al. 2009](#); [Miyoshi et al. 2014](#)). This approach is based on the assumption that comprehensive GCMs can capture a significant portion of GW sources and the details of wave propagation. Thus, they provide a realistic surrogate for observations.

The first high-resolution GCM for Mars has been reported by [Takahashi et al. \(2008\)](#), however, GWs have not been considered explicitly at that time. The only other high-resolution MGCM has been presented by [Miyoshi et al. \(2011\)](#). They performed simulations with a horizontal resolution of  $2 \times 2$  degrees, and analyzed spatio-temporal spectra of the resolved fields. The major finding of their work was an enhancement of wave energy for harmonics with zonal wavenumbers  $s$  up to 30 at tidal frequencies at heights where diurnal and semidiurnal tides are large. Our paper further addresses the lack of knowledge of GW fields in the Martian atmosphere with the new high-resolution ( $\sim 1.1$  degrees in horizontal) MGCM, and directly focuses on smaller-scale ( $s > 60$ ) harmonics, which usually have to be parameterized.

The paper is structured as follows. The high-resolution MGCM is described in Section 2. GW variations in the lower atmosphere (10–30 km) are presented and compared with observations in Section 3. Vertical propagation of GWs is discussed in Section 4, while horizontal distributions of their characteristics are given in Section 5.

## 2. GRAVITY-WAVE RESOLVING MARTIAN GENERAL CIRCULATION MODEL

The high-resolution MGCM used in this study is based on the atmospheric component of the MIROC (Model for Interdisciplinary Research On Climate) terrestrial GCM developed collaboratively by the Atmosphere and Ocean Research Institute (AORI), The University of Tokyo, the National Institute of Environmental Studies (NIES), and the Japan Agency for Marine-Earth Science and Technology (JAMSTEC) in Japan ([K-1 Model Developers 2004](#); [Sakamoto et al. 2012](#)). It utilizes a spectral solver for the three-dimensional primitive equations, and has a set of physical parameterizations appropriate for the Martian atmosphere as described in the works by [Kuroda et al. \(2005, 2013\)](#). The MGCM accounts, among others, for radiative effects of gaseous carbon dioxide and airborne dust, and interactively simulates condensation and sublimation of the atmospheric CO<sub>2</sub>, formation of CO<sub>2</sub> ice clouds, snowfalls and seasonal ice cap in the polar atmosphere. The lower-resolution version of the MGCM has been validated against the observed zonal mean climatology ([Kuroda et al. 2005](#)), and extensively been used for studies of baroclinic planetary waves ([Kuroda et al. 2007](#)), zonal-mean variability in the middle- and high-latitudes ([Yamashita et al. 2007](#)), equatorial semiannual oscillations ([Kuroda et al. 2008](#)), winter polar warmings during global dust storms ([Kuroda et al. 2009](#)), and CO<sub>2</sub> snowfalls in the northern winter polar atmosphere

([Kuroda et al. 2013](#)). Recently, this model received the name DRAMATIC (Dynamics, RAdiation, MAterial Transport and their mutual InterACtions) MGCM, and has been used to validate the retrieved temperature in the southern polar night from the MGS radio occultation measurements ([Noguchi et al. 2014](#)).

In this study, the MGCM was run at the T106 spectral truncation, which corresponds approximately to a  $1.1^\circ \times 1.1^\circ$  (or  $\sim 60$  km) horizontal resolution. In the vertical direction, the model domain extends from the surface to  $\sim 80$ – $100$  km, and is represented by 49  $\sigma$ -levels. Such setup allows for realistically capturing generation and propagation of GWs with horizontal wavelengths of  $3\Delta x \sim 180$  km and longer and, to some extent, their vertical attenuation due to nonlinear processes. These waves are subgrid-scale in conventional GCMs, and the dynamical and thermal importance in the Martian atmosphere of the harmonics of these scales has been demonstrated in the works of [Medvedev et al. \(2011b\)](#) and [Medvedev and Yiğit \(2012\)](#), correspondingly.

The local thermodynamic equilibrium was assumed for the radiative effects of CO<sub>2</sub> gas at all heights.

## 3. GRAVITY WAVE VARIATIONS IN THE LOWER (10-30 KM) ATMOSPHERE

The results shown here are for the Northern Hemisphere winter solstice, i. e., when Mars is at perihelion, and the dynamical processes in the atmosphere are most active. All the figures are based on 20-sol averaged fields centered at the solar longitude  $L_s = 270^\circ$ , with the dust opacity of  $\sim 1.0$  in the visible wavelength (a “low dust” condition).

We designate the shortest horizontal-scale fluctuations with the total wavenumber  $n > 61$  (horizontal wavelengths less than  $\sim 350$  km) as wave disturbances  $\varphi'$ . This choice allows for explicitly considering harmonics, which are known to significantly contribute to dynamical and thermal forcing of large-scale atmospheric flows, and which are usually parameterized in GCMs. Correspondingly, the larger-scale ( $n \leq 60$ ) fields here represent the “mean”  $\bar{\varphi}$  such that  $\varphi = \bar{\varphi} + \varphi'$ . Similar definition is applicable to disturbance covariances. For instance,  $\overline{\varphi'\psi'}$  is the product of shorter-scale fields  $\varphi$  and  $\psi$  on the globe, of which only the lower- $n$  portion is taken. Effectively, averaging denoted by overbars is a horizontal spatial averaging, or a coarse-graining.

Direct measures of activity of fluctuating fields, which we believe are composed mainly of gravity waves, are their kinetic and potential energy (per unit mass)  $E_k$  and  $E_p$ , correspondingly:

$$E_k = \frac{1}{2} \left( \overline{u'^2} + \overline{v'^2} \right), \quad E_p = \frac{1}{2} \left( \frac{g}{N} \right)^2 \frac{\overline{T'^2}}{\overline{T^2}}, \quad (1)$$

where  $u'$  and  $v'$  are the wind fluctuations in the zonal and meridional directions, respectively,  $g$  is the acceleration of gravity, and  $N$  is the Brunt-Väisälä frequency. The quantities  $E_k$  and  $E_p$  averaged between 10 and 30 km are shown in Figures 1a and 1b. This representation allows for a direct comparison with the measurements of GW temperature fluctuations derived from MGS occultation data for the same season ([Creasey et al. 2006a](#), Figure 4b). Their observations show a gradual increase of  $E_p$  in the Southern Hemisphere from  $< 2$  J kg<sup>-1</sup> at

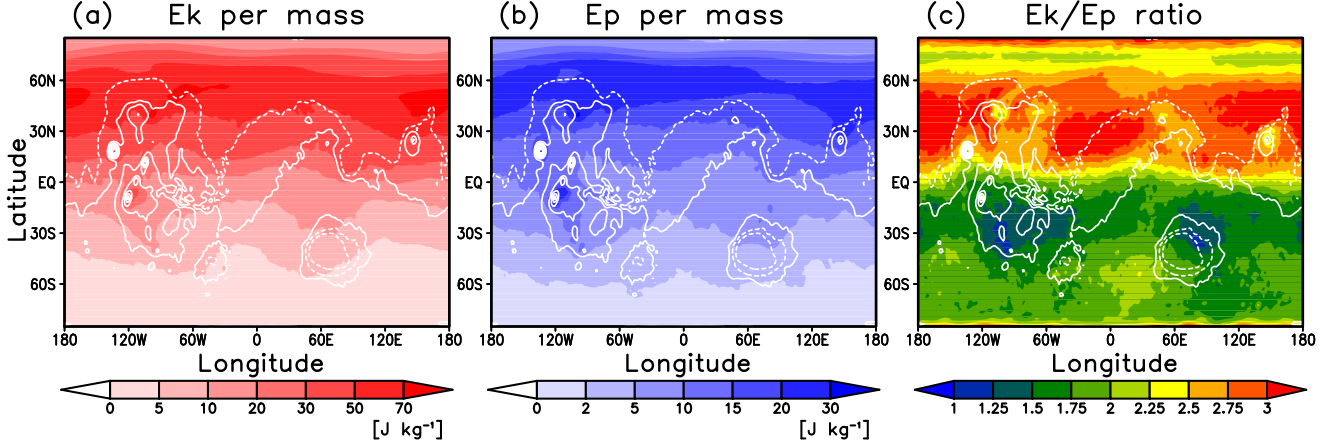


**Figure 1.** (a) Kinetic  $E_k$  and (b) potential energy  $E_p$  per unit mass (in  $\text{J kg}^{-1}$ ) of resolved gravity waves with the total wavenumbers greater than 60 (horizontal wavelengths of less than  $\sim 350$  km), and (c) the ratio  $E_k/E_p$ , averaged between 10 and 100 Pa for 20 sols starting at  $L_s=270^\circ$ . White contours on each plot denote the Martian topography.

high-latitudes to  $10\text{--}15 \text{ J kg}^{-1}$  and larger over the equator, which is in an excellent agreement with our simulations in Figure 1b. Measurements are missing for latitudes higher than  $20^\circ\text{N}$ , where simulations predict an increase of GW activity, and reaches its maximum (of greater than  $30 \text{ J kg}^{-1}$ ) over the core of the westerly polar night jet (at  $\sim 60^\circ$ ). Another observational constraint have been presented by [Wright \(2012\)](#), who derived temperature fluctuations from the Mars Climate Sounder (MCS) data. Although they were obtained for spatial scales longer than in our simulations, the magnitudes of variations are in a very good agreement between 100 and 10 Pa (several K) ([Wright 2012](#), Figure 2a). Observations also show an enhancement of temperature fluctuations in the Northern high-latitudes. In the Southern Hemisphere, our simulations do not reproduce large temperature fluctuations. In addition, [Ando et al. \(2012\)](#) showed that the equatorial region has larger  $E_p$  than any other latitude region, whereas our simulations display that this peak is shifted to the middle latitudes of the Northern Hemisphere.

The distribution of  $E_k$  in Figure 1a is similar to that of  $E_p$ . It also demonstrates the latitudinal asymmetry of gravity wave activity in the lower atmosphere with the maximum in the winter hemisphere. There is an equipartition of kinetic energy between the zonal and meridional components of small-scale wind variations. The results in Figure 1a indicate that the magnitudes of wind fluctuations increase from  $\sim 1 \text{ m s}^{-1}$  in high latitudes of the Southern Hemisphere to  $\sim 6 \text{ m s}^{-1}$  in the middle- and high latitudes of the Northern Hemisphere. These distributions of  $E_p$  and  $E_k$  clearly reflect GW sources in the lower atmosphere.

One property of the small horizontal-scale wave field can immediately be found by comparing  $E_k$  and  $E_p$ : the kinetic component of energy exceeds that of potential energy. [Geller and Gong \(2010, Equation \(10\)\)](#) have derived the relation between the  $E_k/E_p$  ratio and the

intrinsic frequency of gravity wave  $\hat{\omega}$ :

$$\frac{E_k}{E_p} = \frac{1 + \left(\frac{f}{\hat{\omega}}\right)^2}{1 - \left(\frac{f}{\hat{\omega}}\right)^2}, \quad (2)$$

where  $f$  is the Coriolis frequency. It follows from (2) that smaller- $\hat{\omega}$  (longer-period in the frame of reference moving with the local wind) GW harmonics have larger  $E_k/E_p$  ratios, while the latter asymptotically approaches unity for high-frequency harmonics. The calculated ratio  $E_k/E_p$  plotted in Figure 1 points out the interhemispheric asymmetry in the distribution of the dominant intrinsic frequencies  $\hat{\omega}$  of resolved small-scale waves: they are a factor of two or more smaller in the winter hemisphere. Given that their horizontal scales are approximately equal throughout the globe, this implies smaller intrinsic horizontal phase velocities  $c - \bar{u}$  of GWs in the Northern Hemisphere. These waves are generated by the meandering strong winter polar jet (large  $\bar{u}$ ), which means that their observed horizontal phase velocities  $c$  (measured with respect to the surface) are, on the contrary, large. A closer consideration of small-scale GW-induced fields, for instance, of the horizontal wind divergence  $\partial u'/\partial x + \partial v'/\partial y$  (see Movie S1 in the Supporting Information), confirms that wave packets move eastward much faster in the winter polar jet region, although somewhat lag the mean zonal winds. This illustrates the bias in the horizontal phase velocities of small-scale GWs in the source region first pointed out in the work by [Medvedev et al. \(1998\)](#) and utilized in the prescribed source spectrum in the GW parameterization studies for Earth ([Yigit et al. 2009](#)) and Mars ([Medvedev et al. 2011b](#)). In the mountainous regions,  $E_k/E_p$  is, on the contrary, small (blue shades in Figure 1c), which indicates large intrinsic/small observed horizontal phase velocities. This means that topographically-induced GWs dominate there, and that the wave packets are “tied up” to the relief features. Movie S1 clearly demonstrates this



phenomenon.

#### 4. VERTICAL PROPAGATION OF GRAVITY WAVES

Having considered GWs in the lower atmosphere, we now turn to their upward propagation. Vertical fluxes of the zonal and meridional momentum,  $\overline{\rho u'w'}$  and  $\overline{\rho v'w'}$ , respectively, are important quantities for examining this. Zonally averaged distributions of the calculated  $\overline{\rho u'w'}$  and  $\overline{\rho v'w'}$  are plotted with color shades in Figures 2a and b, respectively, and the mean zonal and meridional winds are superimposed with contour lines. The fluxes are vector quantities, which are conserved if no sources and sinks are present. For a given GW harmonic, the momentum flux is proportional to the intrinsic phase velocities in the corresponding direction, and characterizes wave propagation with respect to the mean flow. Only in the absence of the latter, the signs indicate the direction of wave propagation with respect to the surface, that is, in the east-west or north-south. These results suggest that, in the lower atmosphere, the fluxes are, generally, directed against the local winds. This means that the spectra of GWs are dominated by harmonics with observed phase velocities  $c$  that are slower than the local wind (“lagging” the flow), or having opposite signs (moving against the flow):  $c < \bar{u}$  if  $\bar{u} > 0$ , and  $c > \bar{u}$  if  $\bar{u} < 0$ . Over the course of vertical propagation, harmonics are selectively dissipated and/or obliterated due to breaking or filtering by the mean wind. The net wave momentum flux is determined by a delicate balance of contributions of “surviving” harmonics from the initial spectrum. Thus, magnitudes and even the sign of the net flux can vary with height. For instance, the apparent increase of the magnitude in low latitudes between 100 and 10 Pa in Figure 2a does not necessarily indicate in situ generation of waves with positive  $\overline{\rho u'w'}$ . Harmonics with  $\overline{\rho u'w'} < 0$  in the incident spectrum are filtered by the easterly wind  $\bar{u} < 0$ , while waves carrying positive fluxes progressively contribute more, because a) their amplitudes grow with height, and b)  $c - \bar{u}$  and the associated momentum flux increase. Above  $\sim 10$  Pa, the opposite occurs. Harmonics with positive flux partly dissipate and deposit their momentum to the mean flow, as we shall discuss below, and partly their contribution decreases (due to the mean zonal wind  $\bar{u}$  weakening) along with the increase of the contribution of waves with negative fluxes. Same can be applied to the local maximum of positive meridional fluxes  $\overline{\rho v'w'} > 0$  over  $\sim 60^\circ\text{N}$  in Figure 2b.

Since wave momentum fluxes are vector quantities they are not fully suitable for characterizing the net field, because harmonics with opposite signs may offset and even cancel contributions of each other. Wave variances provide another proxy for wave activity, which is devoid of this limitation. Figures 2c and d show their zonal mean latitude-altitude distributions in the form of kinetic and potential energy,  $E_k$  and  $E_p$  from (1), multiplied by the mean density.  $\rho E_k$  exceeds  $\rho E_p$  everywhere in the atmosphere, as it does at lower altitudes in Figure 1. The maximum of wave energy is in the lower atmosphere, where these waves are mainly excited, and decreases with height in each vertical column. However, a clear asymmetry between the Northern and Southern Hemispheres is seen. Wave activity is stronger, and GWs penetrate higher in

the winter hemisphere. Partially, this may be explained by the asymmetry of sources in the lower atmosphere, but refractive properties of the atmosphere associated with the mean winds are likely to play a role as well. Spectra of generated waves in average, are dominated by harmonics with slower phase velocities, as otherwise would cause an “ultraviolet catastrophe” (integral of energy over spectrum diverges). These waves are less affected by strong winds in the core of the westerly jet, and, therefore, are being focused into it. One more reason for the asymmetry can be related to the oblique propagation: wave packets composed of harmonics with slower phase velocities can cover significant horizontal distances upon their vertical propagation. We cannot diagnose the degree of obliqueness directly from the GCM output, and a ray tracing model is required for that. Most likely, all three factors contribute to the obtained distributions of GW activity in the middle atmosphere. Here we simply state that the simulated asymmetry awaits a validation with observations, and that any successful parameterization of subgrid-scale GWs must reproduce it.

Figures 2a and b show that momentum fluxes ultimately decrease with height. Divergence of the momentum fluxes quantifies the rate of wave obliteration, and the amount of momentum transferred to the mean (larger-scale in our study) flow. Depending on the sign, waves can produce acceleration or deceleration of the latter. Figures 3a and b present thus calculated forcing along the corresponding axes:

$$a_x = -\nabla \cdot \overline{\mathbf{v}'u'}, \quad a_y = -\nabla \cdot \overline{\mathbf{v}'v'}, \quad (3)$$

where  $\mathbf{v}' = (u', v', w')$  are the components of velocity fluctuations, and  $\nabla = (\partial/\partial x, \partial/\partial y, \rho^{-1}\partial\rho/\partial z)$ . As can be seen,  $a_x$  and  $a_y$  created by the resolved small-scale motions are significant in the middle atmosphere (tens of  $\text{m s}^{-1} \text{ sol}^{-1}$ ), and directed mainly against the mean wind. This result is consistent with the estimates of GW drag obtained using the extended spectral parameterization of Yigit et al. (2008) applied to the distributions of wind and temperature from the Mars Climate Database (Medvedev et al. 2011a), and interactively coupled with the Martian GCM (Medvedev et al. 2011b). One may notice that it is significantly smaller than the estimates of Fritts et al. (2006) ( $\sim 1000$  of  $\text{m s}^{-1} \text{ sol}^{-1}$ ), but it is because we present zonal and time averaged quantities, while their results are based on individual measurements. Instantaneously,  $a_x$  and  $a_y$  in our simulations can reach over  $10\,000 \text{ m s}^{-1} \text{ sol}^{-1}$ . The response of the mean zonal winds to this forcing is also seen – the jets show the tendency to decrease and close in the upper portion of the domain. This cannot be achieved in simulations with conventional (low) resolution without parameterized subgrid-scale GWs, unless an artificial sponge layer is applied near the top. Thus, our GW-resolving simulations represent a direct confirmation of the predictions on the dynamical importance and effects of small-scale GWs in the Martian atmosphere.

The plotted divergences further illustrate GW propagation in the equatorial region. They show weak negative  $a_x$  below 10 Pa created by the absorption of harmonics with negative fluxes by the easterly mean wind  $\bar{u} < 0$ , as is discussed above. Around 10 Pa, strong dissipation of harmonics with  $\overline{u'w'} > 0$  produces positive  $a_x$  decelerat-

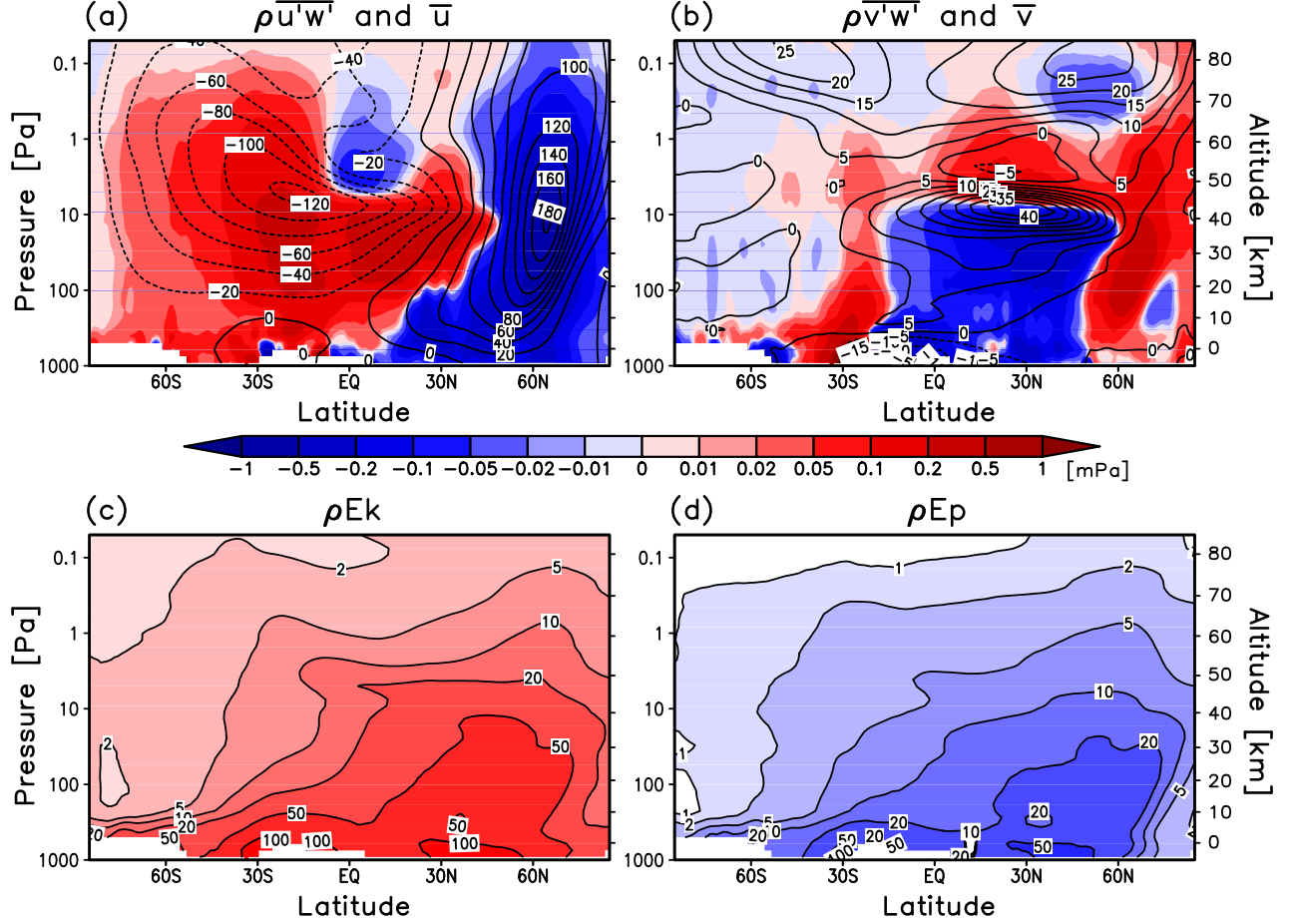


**Figure 2.** The latitude-altitude cross-sections of zonal-mean quantities due to resolved GWs with the total wavenumber of larger than 60 (shaded): (a) vertical flux of zonal wave momentum  $\rho \overline{u'w'}$  (in mPa), (b) vertical flux of meridional momentum  $\rho \overline{v'w'}$ , (c) kinetic wave energy  $\rho E_k$  (in  $\text{mJ m}^{-3}$ ), (d) potential wave energy  $\rho E_p$ . Black contours in (a) represent the zonal wind (in  $\text{m s}^{-1}$ ), and the meridional wind in (b).

ing the mean wind. Above 10 Pa, the remaining harmonics with negative fluxes deposit the negative momentum upon their dissipation, which results in the acceleration of the negative flow. The latter seems paradoxical as all the waves with negative fluxes should have apparently been filtered below by the negative background wind. An in depth explanation of such phenomenon was given in the paper of *Yigit et al. (2009, Section 8, paragraph 42 and Figure 8)*, and is related to the fact that the projection of the wind on the direction of wave propagation (that affects the latter) can significantly differ from the zonal wind alone.

The vertically alternating patches of positive and negative  $a_x$  in the equatorial region tend to enhance the semiannual oscillation of the zonal wind, as discussed in the work of *Kuroda et al. (2008)*. The meridional component of the GW-induced torque,  $a_y$ , also plays an important role in the middle atmosphere. It decelerates the cross-equatorial south-to-north meridional transport in low and middle latitudes at  $\sim 10$  Pa induced mainly by thermal tides, accelerates it somewhat higher (at  $\sim 1$  Pa), and extends to high latitudes of the winter (Northern) hemisphere. This leads to the intensification of the downward branch of the meridional transport cell

over the North Pole, which results in the increase of the adiabatic heating and enhancement of the middle atmosphere polar warming (*Medvedev and Hartogh 2007; Kuroda et al. 2009*). Similarly, small-scale GWs decelerate the northward meridional flow in the upper mesosphere, and weaken the meridional pole-to-pole cell.

Next, we estimate the contributions of the vertical component of the momentum flux divergence to the net  $a_x$  and  $a_y$  by plotting  $-\rho^{-1}d\rho \overline{u'w'}/dz$  and  $-\rho^{-1}d\rho \overline{v'w'}/dz$  in Figures 3c and d. They are very close to those in Figures 3a and b. This indicates that a) horizontal propagation of GWs plays a secondary role in forcing the mean flow, and b) GW parameterizations accounting for only vertical propagation can successfully capture the major part of subgrid-scale GW effects in GCMs.

## 5. HORIZONTAL DISTRIBUTIONS OF WAVE FLUXES

Many parameterizations use wave momentum fluxes at a certain level in the lower atmosphere for the specification of sources. Therefore, we plotted the longitude-latitude distributions of  $\overline{u'w'}$  and  $\overline{v'w'}$  at  $p = 260$  Pa

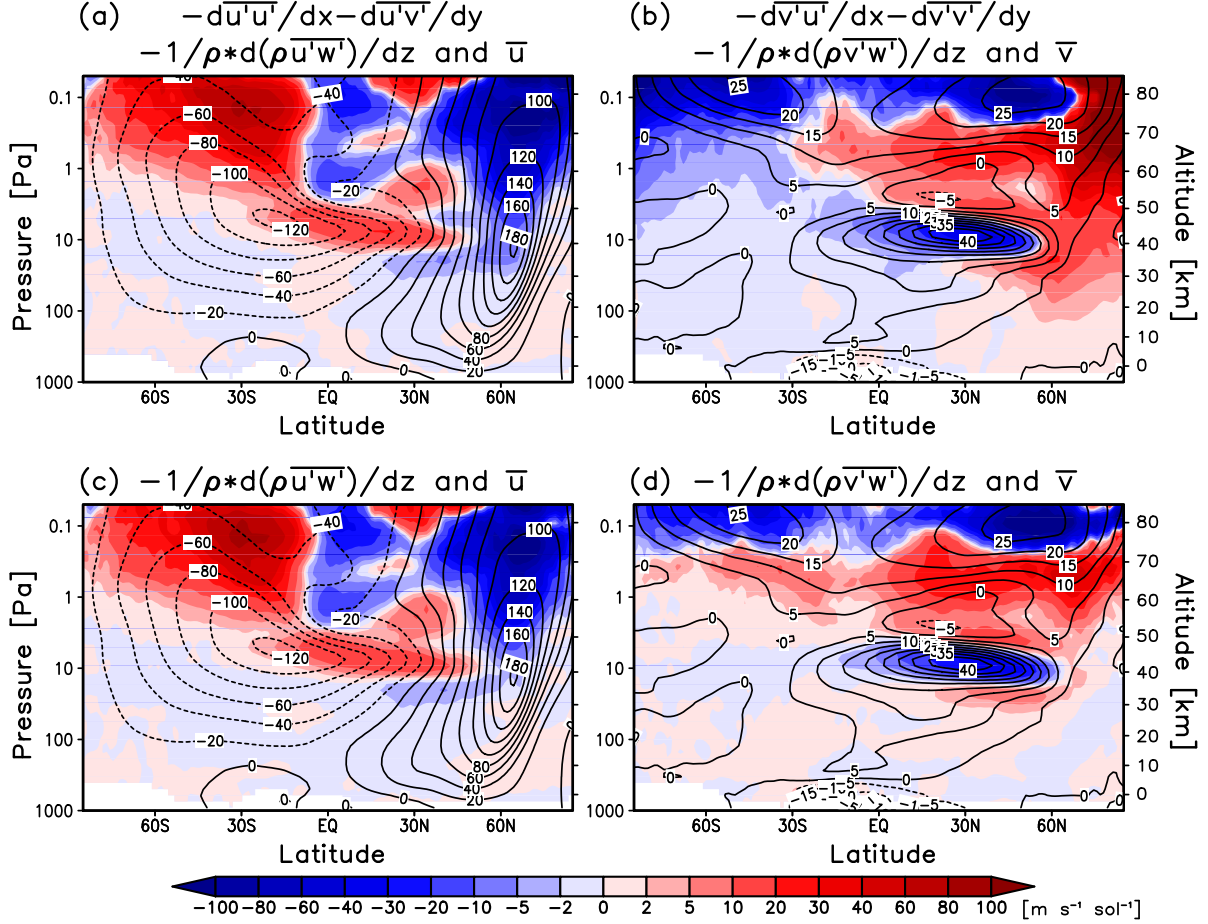


**Figure 3.** The components of divergences of gravity wave momentum fluxes (shaded, in  $\text{m s}^{-1} \text{ sol}^{-1}$ ) and the mean wind (contours, in  $\text{m s}^{-1}$ ): full (horizontal and vertical) divergences of (a) zonal and (b) meridional momentum fluxes; only vertical divergence of (c) zonal and (d) meridional momentum fluxes. Black contours denote (a, c) the mean zonal, and (b, d) meridional wind.

in Figures 4a–b. They are shown with color shades, and the corresponding large-scale winds  $\bar{u}$  and  $\bar{v}$  are superimposed with contours. Although all quantities are 20-day averaged, fluxes are seen to be very patchy, which demonstrates that sources are extremely localized both in space and time. Peak values of the fluxes with alternating signs occur in the mountainous regions. They are evidently associated with waves generated by flow over topography. Nevertheless, a clear asymmetry can be seen: fluxes predominantly have signs opposite to the mean local wind. In the middle- to high-latitudes of the Northern Hemisphere, the distribution of the zonal flux is significantly smoother. These GWs are excited within the curvatures of the winter westerly jet, which, in large, are associated with Kelvin waves moving eastward with time. The meridional fluxes are negative and directed against the mean meridional wind between the Equator and  $45^\circ\text{N}$ , and have alternating direction in other regions, where the mean wind is weak.

For comparison, the zonal momentum fluxes created by harmonics penetrating to the mesosphere ( $p = 0.1$  Pa) are shown in Figure 4c. Their distribution is significantly more horizontally homogeneous. Most orographic GWs (with small with respect to the surface phase speeds) are filtered out by the wind in the course of their vertical

propagation, and create only a marginal enhancement over the mountainous regions. This confirms the fact well-known from Earth studies that GWs with progressively faster horizontal phase speeds dominate at high altitudes (Yigit and Medvedev 2015). The region with negative (but large) horizontal wave momentum fluxes in the mesosphere is confined to Northern high-latitudes, which reflects the favorable propagation conditions for the corresponding harmonics, and which is in line with our finding using the GW parameterization (Medvedev et al. 2011b; Yigit et al. 2015). The magnitudes of fluxes in the mesosphere significantly exceed those in the lower atmosphere, which merely reflects the wave amplitude growth due to exponential density drop with height.

Finally, we show the calculated vertical divergence of momentum fluxes (wave drag),  $a_x = -\rho^{-1}d(\rho u'w')/dz$ , in the mesosphere (Figure 4d). It is consistent with the zonal mean cross-section in Figure 2d, but shows a high degree of horizontal inhomogeneity. Locally,  $a_x$  exceeds  $200 \text{ m s}^{-1} \text{ sol}^{-1}$  at  $p = 0.1$  Pa, but almost nowhere is less than several tens of  $\text{m s}^{-1} \text{ sol}^{-1}$ . Obviously, such strong effects of small-scale waves cannot be ignored in the dynamics of the Martian mesosphere. Note that the values and distributions of both wave fluxes and acceler-



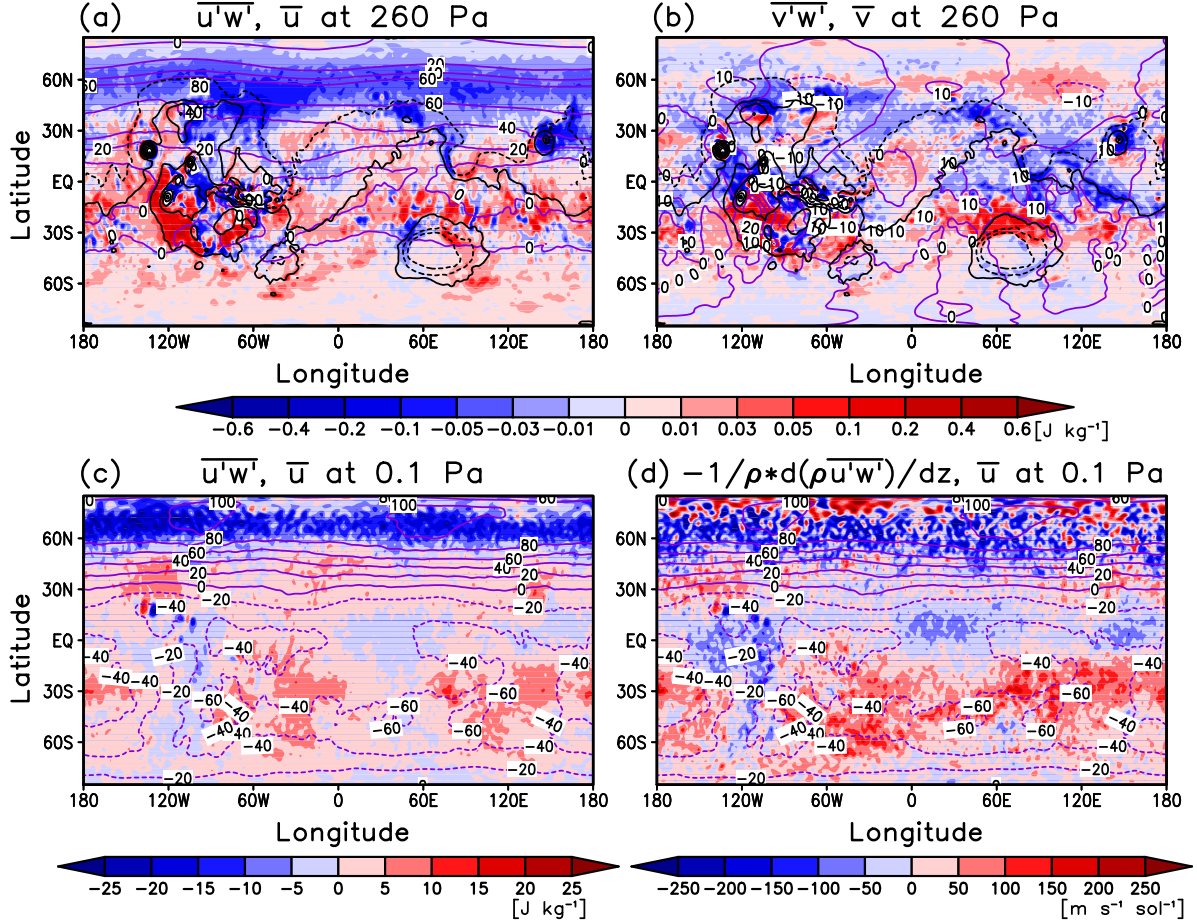


**Figure 4.** The distribution of horizontal flux of zonal wave momentum  $\overline{u'w'}$  at (a) 260 Pa and (c) 0.1 Pa pressure levels (shaded, in  $\text{J kg}^{-1}$ ). Black contours represent the topography of Mars. (b) The same as in (a) except for  $\overline{v'w'}$ . (d) The divergence of meridional wave momentum (in  $\text{m s}^{-1} \text{ sol}^{-1}$ ) at 0.1 Pa pressure level. Black contours in (a) and (b) represent the topographical features. Purple contours in (a), (c) and (d) denote the mean zonal wind velocity  $\bar{u}$  (in  $\text{m s}^{-1}$ ), while in (b) denote the mean meridional wind velocity  $\bar{v}$ .

ation/deceleration obtained in this high-resolution simulation can and should be served for validation and tuning of GW parameterizations.

## 6. CONCLUSIONS

We presented the first results of simulations with a new high-resolution Martian general circulation model (triangle spectral truncation T106) that resolves (in a  $3\Delta x$  sense) harmonics with horizontal scales down to  $\sim 180$  km. In this paper, we concentrated on the Northern winter solstice (around the solar longitude  $L_s = 270^\circ$ ) and GW harmonics shorter than 350 km. This consideration leaves aside shorter-scale (few tens of km) harmonics generated by convection, and which can be important in the upper atmosphere. The main inferences of this first study of its kind are listed below.

1. Magnitudes of temperature variances due to small-scale GWs (or available potential wave energy  $E_p$ ) between 10 and 30 km are in a good agreement with those obtained by [Creasey et al. \(2006a\)](#) from Mars Global Surveyor radio occultation data. In addition, simulations show a gradual and steep latitudinal increase of  $E_p$  from South to North with

the maximum in the winter hemisphere, where the observational data are missing.

2. Variances of wave-induced horizontal wind fluctuations exhibit a similar behavior, however, with a steeper growth – the ratio of the wave kinetic and potential energy,  $E_k/E_p$ , increases from  $\sim 1.5$  in the Southern Hemisphere to about 3 in the Northern one.
3. Two major sources of GWs can be identified in the lower atmosphere: the mountainous regions generating slow, or even non-moving with respect to the surface wave packets, and the meandering winter westerly jet exciting faster GW harmonics traveling mainly eastward.
4. The majority of generated GWs move slower than the background wind, and the associated vertical fluxes of horizontal wave momentum are directed against it.
5. Most of GWs are produced in the lower atmosphere, and their fluxes and energy decay with height.

6. Upon vertical propagation and dissipation, these waves deposit their momentum directed mainly against the local wind, and, thus, provide a wave drag on the mean flow.
7. As a result of the drag, the simulated jets in both hemispheres demonstrate a tendency to close in the upper atmosphere. This feature cannot be reproduced by GCMs with a conventional (low) resolution without applying an artificial sponge near the model top or an appropriate GW parameterization.
8. In the lower atmosphere, the distributions of wave momentum fluxes are very patchy, reflecting the highly localized nature of GW sources. Orographically generated slow waves are filtered in lower layers in the course of their vertical propagation, and the upper mesosphere is dominated by harmonics with faster horizontal phase velocities.

Given the lack of observations of GWs in the atmosphere of Mars, our high-resolution simulations provide the much needed framework for constraining GW parameterizations, and validating the results obtained with the latter.

Data supporting the figures are available from TK (tkuroda@pat.gp.tohoku.ac.jp).

TK was supported by the Japan Society for the Promotion of Science (JSPS) KAKENHI Grant Number 24740317, and the Promotion of the Strategic Research Program for Overseas Assignment of Young Scientists and International Collaborations titled "Intensification of International Collaborations for Planetary Plasma and Atmospheric Dynamics Research based on the Hawaiian Planetary Telescopes". The model runs have been performed with the HITACHI SR16000 System (yayoi) at the Information Technology Center, The University of Tokyo. This work was partially supported by German Science Foundation (Deutsche Forschungsgemeinschaft) grant ME2752/3-1 and NASA grant NNX13AO36G.

## REFERENCES

- Alexander, M. J., and 15 coauthors Recent developments in gravity wave effects in climate models, and the global distribution of gravity wave momentum flux from observations and models, *Q. J. Roy. Meteorol. Soc.*, **136**, 1103–1124.
- Ando, H., T. Imamura, and T. Tsuda (2012), Vertical wavenumber spectra of gravity waves in the Martian atmosphere obtained from Mars Global Surveyor radio occultation data, *J. Atmos. Sci.*, **69**, 2906–2912.
- Creasey, J. E., J. M. Forbes, and D. P. Hinson (2006a), Global and seasonal distribution of gravity wave activity in Mars' lower atmosphere derived from MGS ratio occultation data, *Geophys. Res. Lett.*, **33**, L01803, doi:10.1029/2005GL024037.
- Creasey, J. E., J. M. Forbes, and G. M. Keating (2006b), Density variability at scales typical of gravity waves observed in Mars' thermosphere by the MGS accelerometer, *Geophys. Res. Lett.*, **33**, L22814, doi:10.1029/2005GL027538.
- Fritts, D. C. and M. J. Alexander (2003), Gravity wave dynamics and effects in the middle atmosphere, *Rev. Geophys.*, **41**, 1003, doi:10.1029/2001RG000106.
- Fritts, D. C., L. Wang, and R. H. Tolson (2006), Mean and gravity wave structures and variability in the Mars upper atmosphere inferred from Mars Global Surveyor and Mars Odyssey aerobraking densities, *J. Geophys. Res.*, **111**, A12304, doi:10.1029/2006JA011897.
- Geller, M. A., and L. Gong (2010), Gravity wave kinetic, potential, and vertical fluctuation energies as indicators of different frequency gravity waves, *J. Geophys. Res.*, **115**, D11111, doi:10.1029/2009JD012266.
- González-Galindo, F., Forget, F., López-Valverde, M.A., Angelats i Colli, M., Millour, E. (2009), A ground-to-exosphere martian general circulation model: 1. Seasonal, diurnal, and solar cycle variation of thermospheric temperatures, *J. Geophys. Res.*, **114**, E04001, doi:10.1029/2008JE003246.
- Hartogh, P., A. S. Medvedev, T. Kuroda, R. Saito, G. Villanueva, A. G. Feofilov, A. A. Kutepov, and U. Berger (2005), Description and climatology of a new general circulation model of the Martian atmosphere, *J. Geophys. Res.*, **110**, E11008, doi:10.1029/2005JE002498.
- Hartogh, P., A. S. Medvedev, and C. Jarchow (2007), Middle atmosphere polar warmings on Mars: simulations and study on the validation with sub-millimeter observations, *Planet. Space Sci.*, **55**, 1103–1112.
- K-1 Model Developers (2004), K-1 coupled GCM (MIROC) description, *K-1 Tech. Rep.*, **1**, pp.1–34, Univ. of Tokyo, Tokyo.
- Kuroda, T., N. Hashimoto, D. Sakai, and M. Takahashi (2005), Simulation of the Martian atmosphere using a CCSR/NIES AGCM, *J. Meteor. Soc. Japan.*, **83**, 1–19.
- Kuroda, T., A. S. Medvedev, P. Hartogh, and M. Takahashi (2007), Seasonal changes of the baroclinic wave activity in the northern hemisphere of Mars simulated with a GCM, *Geophys. Res. Lett.*, **34**, L09203, doi:10.1029/2006GL028816.
- Kuroda, T., A. S. Medvedev, P. Hartogh, and M. Takahashi (2008), Semiannual oscillations in the atmosphere of Mars, *Geophys. Res. Lett.*, **34**, L23202, doi:10.1029/2008GL036061.
- Kuroda, T., A. S. Medvedev, P. Hartogh, and M. Takahashi (2009), On forcing the winter polar warmings in the Martian middle atmosphere during dust storms, *J. Meteor. Soc. Japan.*, **87**, 913–921.
- Kuroda, T., A. S. Medvedev, Y. Kasaba and P. Hartogh (2013), Carbon dioxide ice clouds, snowfalls, and baroclinic waves in the northern winter polar atmosphere of Mars, *Geophys. Res. Lett.*, **40**, 1484–1488.
- Medvedev, A. S., and P. Hartogh (2007), Winter polar warmings and the meridional transport on Mars simulated with a general circulation model, *Icarus*, **186**, 97–110.
- Medvedev, A. S., G. P. Klaassen, and S. R. Beagley (1998), On the role of an anisotropic gravity wave spectrum in maintaining the circulation of the middle atmosphere, *Geophys. Res. Lett.*, **25**, 509–512.
- Medvedev, A. S., E. Yiğit, and P. Hartogh (2011a), Estimates of gravity wave drag on Mars: Indication of a possible lower thermospheric wind reversal, *Icarus*, **211**, doi:10.1016/j.icarus.2010.10.013, 909–912.
- Medvedev, A. S., E. Yiğit, P. Hartogh, and E. Becker (2011b), Influence of gravity waves on the Martian atmosphere: General circulation modeling, *J. Geophys. Res.*, **116**, E10004, doi:10.1029/2011JE003848.
- Medvedev, A. S., E. Yiğit, T. Kuroda, and P. Hartogh (2013), General circulation modeling of the martian upper atmosphere during global dust storms, *J. Geophys. Res.*, **118**, 2234–2246, doi:10.1002/jgre.20163.
- Medvedev, A. S., F. González-Galindo, E. Yiğit, A. G. Feofilov, F. Forget, and P. Hartogh (2015), Cooling of the Martian thermosphere by CO<sub>2</sub> radiation and gravity waves: An intercomparison study with two general circulation models, *J. Geophys. Res. Planets*, **120**, 913–927, doi:10.1002/2015JE004802.
- Medvedev, A. S., and E. Yiğit (2012), Thermal effects of internal gravity waves in the Martian upper atmosphere, *Geophys. Res. Lett.*, **39**, L05201, doi:10.1029/2012GL050852.
- Miyoshi, Y., J. M. Forbes, and Y. Moudén (2011), A new perspective on gravity waves in the Martian atmosphere: Sources and features, *J. Geophys. Res. Planets*, **116**, E09009, doi:10.1029/2011JE003800.
- Miyoshi, Y., H. Fujiwara, H. Jin, and H. Shinagawa (2014), A global view of gravity waves in the thermosphere simulated by a general circulation model, *J. Geophys. Res. Space Physics*, **119**, 5807–5820, doi:10.1002/2014JA019848.
- Noguchi, K., S. Ikeda, T. Kuroda, S. Tellmann, and M. Pätzold (2014), Estimation of changes in the composition of the Martian atmosphere caused by CO<sub>2</sub> condensation from GRS Ar measurements and its application to the re-derivation of MGS radio occultation measurements, *J. Geophys. Res. Planets*, **119**, doi:10.1002/2014JE004629.
- Sakamoto, T. T., et al. (2012), MIROC4h-A New High-Resolution Atmosphere-Ocean Coupled General Circulation Model, *J. Meteor. Soc. Japan.*, **90**, 325–359.
- Sato, K., S. Watanabe, Y. Kawatani, Y. Tomikawa, K. Miyazaki, and M. Takahashi (2009), On the origins of mesospheric gravity waves, *Geophys. Res. Lett.*, **36**, L19801, doi:10.1029/2009GL039908.



- Takahashi, Y.O., Y.-Y. Hayashi, M. Odaka, and W. Ohfuchi (2008), High Resolution Simulations of the General Circulation of the Martian Atmosphere: Small and Medium Scale Disturbances and Dust Lifting Processes, Third International Workshop on the Mars Atmosphere: Modeling and Observations, Williamsburg, VA, 2008, Edited by F. Forget, M. A. Lopez-Valverde, S. R. Lewis, P. L. Read and R. J. Wilson. *Publisher: LMD, IAA, AOPP, CNES, ESA*.
- Watanabe, S., Y. Kawatani, Y. Tomikawa, K. Miyazaki, M. Takahashi, and K. Sato (2008), General aspects of a T213L256 middle atmosphere general circulation model, *J. Geophys. Res. Atmospheres*, *113*, D12110, doi:10.1029/2008JD010026.
- Wright, C. J. (2012), A one-year seasonal analysis of martian gravity waves using MCS data, *Icarus*, *219*, 274–282.
- Yamashita, Y., T. Kuroda and M. Takahashi (2007), Maintenance of zonal wind variability associated with the annular mode on Mars, *Geophys. Res. Lett.*, *34*, L16819, doi:10.1029/2007GL030069.
- Yiğit, E., and A. S. Medvedev (2009), Heating and cooling of the thermosphere by internal gravity waves, *Geophys. Res. Lett.*, *36*, L14807, doi:10.1029/2009GL038507.
- Yiğit, E., and A. S. Medvedev (2012), Gravity waves in the thermosphere during a sudden stratospheric warming, *Geophys. Res. Lett.*, *39*, L21101, doi:10.1029/2012GL053812.
- Yiğit, E., and A. S. Medvedev (2015), Internal wave coupling processes in Earth's atmosphere, *Adv. Space Res.*, *55*, doi:10.1016/j.asr.2014.11.020, 983–1003.
- Yiğit, E., A. D. Aylward, and A. S. Medvedev (2008), Parameterization of the effects of vertically propagating gravity waves for thermosphere general circulation models: Sensitivity study, *J. Geophys. Res.*, *113*, D19106, doi:10.1029/2008JD010135.
- Yiğit, E., A. S. Medvedev, A. D. Aylward, P. Hartogh, and M. J. Harris (2009), Modeling the effects of gravity wave momentum deposition on the general circulation above the turbopause, *J. Geophys. Res.*, *114*, D07101, doi:10.1029/2008JD011132.
- Yiğit, E., A. S. Medvedev, A. D. Aylward, A. J. Ridley, M. J. Harris, M. B. Moldwin, and P. Hartogh (2012), Dynamical effects of internal gravity waves in the equinoctial thermosphere, *J. Atmos. Sol.-Terr. Phys.*, *90–91*, 104–116, doi:10.1016/j.jastp.2011.11.014.
- Yiğit, E., A. S. Medvedev, S. L. England, and T. J. Immel (2014), Simulated variability of the high-latitude thermosphere induced by small-scale gravity waves during a sudden stratospheric warming, *J. Geophys. Res.*, *119*, doi:10.1002/2013JA019283.
- Yiğit, E., A. S. Medvedev, and P. Hartogh (2015), Gravity waves and high-altitude CO<sub>2</sub> ice cloud formation in the Martian atmosphere, *Geophys. Res. Lett.*, *42*, doi:10.1002/2015GL064275.